Acta Materialia 274 (2024) 120036

Contents lists available at ScienceDirect

Acta Materialia

journal homepage: www.elsevier.com/locate/actamat

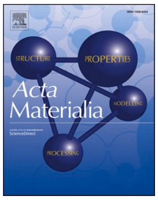

Full length article

Influence of austenite grain boundary misorientation on hydrogen-induced intergranular crack propagation in a medium carbon martensitic steel

Ji Hoon Kim [a,*], Goro Miyamoto [a], Akinobu Shibata [b], Tomohiko Hojo [c], Motomichi Koyama [a], Yongjie Zhang [a], Tadashi Furuhara [a,1]

[a] Institute for Materials Research (IMR), Tohoku University, 2-1-1 Katahira Aoba-Ku, Sendai 980-8577, Japan
[b] Research Center for Structural Materials, National Institute for Materials Science (NIMS), 1-2-1, Sengen, Tsukuba, 305-0047, Japan
[c] Tohoku Gakuin University, 3-1 Shimizukoji Wakabayashi-Ku, Sendai Miyagi, 984-8588 Japan, 980-0812, Japan

ARTICLE INFO

Keywords:
Hydrogen embrittlement
Intergranular fracture
Prior austenite grain boundary (PAGB)
Misorientation angle
Martensite variant selection

ABSTRACT

This study investigated the influence of austenite misorientation (θ_γ) on hydrogen-induced intergranular cracking along the prior austenite grain boundary (PAGB) in a medium C tempered martensitic steel. Utilizing EBSD analysis and prior austenite orientation reconstruction, distributions of martensite misorientation ($\theta_{\alpha'}$) and prior austenite misorientation (θ_γ) across PAGBs were compared in both fractured and total PAGBs. The comparison suggests that presence of low misorientation martensite segments ($\theta_{\alpha'} < 10^\circ$) at PAGB was beneficial to suppress PAGB cracking in accordance with the previous study. This low misorientation martensite segments are more likely to be achieved when θ_γ is either less than 10° (L-PAGB), or over 45° (H-PAGB) with a specific condition. The requirements for H-PAGB to achieve low misorientation martensite segment were investigated by applying interrupt quenching treatment, which can capture the initial nucleation of martensite. The result suggests that the nucleated martensite should hold near Kurdjumov-Sachs orientation relationship (KS OR) not only with austenite into which it grows, but also with opposite austenite sharing the grain boundary (double KS OR) to achieve low misorientation martensite segments. The double KS OR is satisfied in most of martensite nucleated in the early stage, indicating the importance of the variant selection to achieve low misorientation martensite segments at PAGB.

1. Introduction

Hydrogen enters and rapidly diffuses in steel during processing and application, resulting in a substantial loss of ductility. This phenomenon is known as hydrogen embrittlement (HE). As the strength of metallic materials increases, the impact of HE becomes more pronounced [1], making it particularly noteworthy amid the rising demand for high-strength steel. Among the various high strength steels, martensitic steel, known for its exceptional strength over 1 GPa, stands out as the most susceptible to HE.

In general, martensitic steel exhibits two distinctive hydrogen-induced fracture modes: quasi-cleavage (QC) fracture [2-6] and intergranular (IG) fracture [5,7-12]. QC fracture is the term used to describe the fractures that occur on near cleavage plane ((110) or (100)) but leaving different characteristic fracture surface such as tear ridges and serrated marking. On the other hand, IG fracture typically occurs in prior austenite grain boundary (PAGB) and is characterized by a flat fracture surface. Notably, the transition from QC fracture to IG fracture is associated with a decrease in fracture stress, signifying the greater severity of IG fracture [4,5,13]. In that sense, suppressing PAGB cracking would be the priority to improve the reliability of martensitic steel.

The hydrogen-related IG fracture has been discussed in terms of hydrogen-enhanced decohesion [14-17], hydrogen-enhanced localized plasticity [14,15,17,18], hydrogen-enhanced strain-induced vacancy [19,20], etc. In the context of decohesion, there are two primary methods to prevent IG fracture along conventional grain boundaries (not PAGB) in polycrystalline metallic materials. One approach is controlling grain boundary segregation. Previous studies have shown that the addition of grain boundary strengthening elements (C, B, and Mo) or the reduction of grain boundary weakening elements (P, Sn, Mn, and Sb) can

---

* Corresponding author.
E-mail address: kim.ji.hoon.e1@tohoku.ac.jp (J.H. Kim).
[1] Tadashi Furuhara was an Editor of the journal during the review period of the article. To avoid a conflict of interest, Tadashi Furuhara was blinded to the record and another editor processed this manuscript.

https://doi.org/10.1016/j.actamat.2024.120036
Received 13 April 2024; Received in revised form 20 May 2024; Accepted 22 May 2024
Available online 23 May 2024

effectively suppress both general [21-27] and hydrogen-assisted [28-30] grain boundary cracking in steel. It has been reported that the extent of boundary segregation is influenced by alloy interactions [31,32] and grain boundary misorientation [33-35]. The other approach involves enhancing intrinsic coherency at the grain boundary by introducing coherent boundaries such as low index $\sum$ boundaries or low misorientation grain boundaries. This approach could also improve general [36,37], liquid metal assisted [38], and hydrogen-assisted [39] grain boundary cracking in steel. The former method has been employed to mitigate PAGB cracking in martensitic steel. Alloy elements that segregate to austenite grain boundaries during austenitization remain after the martensitic transformation, affecting PAGB cohesion. For instance, Yoo et al. reported improved HE resistance in 32MnB5 hot-stamping steel with the addition of Mo [40]. Mo segregated to PAGB enhanced PAGB cohesion, suppressing PAGB cracking. Okada et al. controlled C segregation at PAGB by varying austenitization temperature in 0.2C-3.0Mn martensitic steel and demonstrated that increasing C segregation at PAGB suppressed the hydrogen-induced PAGB cracking [9]. However, the latter method (increasing population of coherent boundary) can hardly be employed since the PAGB is not a conventional homogeneous grain boundary but consists of several martensite boundary segments with various misorientations of martensite ($\theta_{\alpha'}$) (supplementary material, Fig. S1). Lath martensite, typically formed in low-alloyed steel, exhibits a Kurdjumov-Sachs orientation relationship (KS OR), specifically, $(111)_\gamma$ // $(011)_{\alpha'}$, $[-101]_\gamma$ // $[-1-11]_{\alpha'}$. A single austenite grain can transform into crystallographically equivalent 24 KS martensite variants (Table 1). This theoretically yields 576 (24 × 24) types of martensite segments with different misorientation characteristic at PAGB.

Regarding effects of crystallography on intergranular crack propagation, Shibata et al. observed hydrogen-induced PAGB crack propagation path in martensitic steel using 3D-X-ray microscopy. They revealed that the crack is reluctant to propagate along the PAGB containing low misorientation martensite segments, even when the applied stress was higher than other PAGBs without low misorientation martensite segments [7,8]. Chen et al. analyzed the grain orientation spread (GOS) values along the hydrogen-induced PAGB crack path and reported that the low misorientation martensite segments can suppress the crack propagation by accommodating more plastic strain [41]. Archie et al. conducted a micro-cantilever bending test at PAGBs with and without low misorientation martensite segments. They revealed that the PAGB with low misorientation martensite segments exhibits greater resistance to crack nucleation [37]. Although those previous studies emphasized the importance of low misorientation martensite segments for preventing PAGB cracking, conditions necessary for a PAGB to exhibit low misorientation martensite segments have not been clarified.

The present authors believe that misorientation of austenite (θ_γ), a basic yet highly influential crystallographic factor, may play a crucial role in preventing PAGB cracking in terms of both grain boundary segregation and coherency based on the two primary reasons. Regarding the correlation between segregation and θ_γ, it has been reported that the amount of segregation increases with increasing θ_γ [33,34]. For the relationship between coherency and θ_γ, the clear orientation relationship (KS OR) between austenite and martensite results in martensite misorientation being dependent on θ_γ. Furthermore, specific misorientation of martensite segments are preferentially formed due to variant selection in nucleation at austenite grain boundary. It has been reported that certain martensite/bainite variant is preferentially selected when it is nucleated at austenite grain boundary [42-44]. Furuhara et al. [42]. proposed variant selection rules, which is governed by near KS OR between bainite/martensite and the adjacent austenite where bainite/martensite does not grow (also referred as double KS OR), relation between GB plane and growth direction, habit plane and shape strain direction. Among them, double KS OR is the most relevant to the formation of low misorientation martensite segment. Therefore, this study aims to investigate the influence of θ_γ on hydrogen-induced PAGB cracking in a medium C tempered martensitic steel.

Table 1
24 KS OR martensite variants and their inter-variant relationship.

Variant Number	Parallel Plane	Parallel Direction	Rotation from Variant 1
V1	$(111)_\gamma//$ $(011)_{\alpha'}$	$[-1\ \ 0\ \ 1]_\gamma//$ $[-1\ \ -11]_{\alpha'}$	–
V2		$[-1\ \ 0\ \ 1]_\gamma//$ $[-1\ \ 1\ \ -1]_{\alpha'}$	[0.58 −0.58 0.58]/60.0 deg
V3		$[01\ \ -1]_\gamma//$ $[-1\ \ -1\ \ 1]_{\alpha'}$	[0.00 −0.71 −0.71]/60.0 deg
V4		$[0\ \ 1\ \ -1]_\gamma//$ $[-1\ \ 1\ \ -1]_{\alpha'}$	[0.00 0.71 0.71]/10.5 deg
V5		$[1\ \ -10]_\gamma//$ $[-1\ \ -1\ \ 1]_{\alpha'}$	[0.58 0.71 0.71]/60.0 deg
V6		$[1\ \ -1\ \ 0]_\gamma//$ $[-1\ \ 1\ \ -1]_{\alpha'}$	[0.00 −0.71 −0.71]/49.5 deg
V7	$(1-11)_\gamma//$ $(011)_{\alpha'}$	$[1\ \ 0\ \ -1]_\gamma//$ $[-1\ \ -1\ \ 1]_{\alpha'}$	[−0.58 −0.58 0.58]/49.5 deg
V8		$[1\ \ 0\ \ -1]_\gamma//$ $[-1\ \ 1\ \ -1]_{\alpha'}$	[0.58 −0.58 0.58]/10.5 deg
V9		$[-1\ \ -1\ \ 0]_\gamma//$ $[-1\ \ -1\ \ 1]_{\alpha'}$	[−0.19 0.77 0.61]/50.5 deg
V10		$[-1\ \ -1\ \ 0]_\gamma//$ $[-1\ \ 1\ \ -1]_{\alpha'}$	[−0.49 −0.46 0.74]/50.5 deg
V11		$[0\ \ 1\ \ 1]_\gamma//$ $[-1\ \ -1\ \ 1]_{\alpha'}$	[0.35 −0.93 −0.07]/14.9 deg
V12		$[0\ \ 1\ \ 1]_\gamma//$ $[-1\ \ 1\ \ -1]_{\alpha'}$	[0.36 −0.71 0.60]/57.2 deg
V13	$(-111)_\gamma//$ $(011)_{\alpha'}$	$[0\ \ -\ \ 11]_\gamma//$ $[-1\ \ -1\ \ 1]_{\alpha'}$	[0.93 0.35 0.07]/14.9 deg
V14		$[0\ \ -1\ \ 1]_\gamma//$ $[-1\ \ 1\ \ -1]_{\alpha'}$	[0.74 0.46 −0.49]/50.5 deg
V15		$[-1\ \ 0\ \ -1]_\gamma//$ $[-1\ \ -1\ \ 1]_{\alpha'}$	[−0.25 −0.63 −0.74]/ 57.2 deg
V16		$[-1\ \ 0\ \ -1]_\gamma//$ $[-1\ \ 1\ \ -1]_{\alpha'}$	[0.66 0.66 0.36]/20.6 deg
V17		$[1\ \ 1\ \ 0]_\gamma//$ $[-1\ \ -1\ \ 1]_{\alpha'}$	[−0.66 0.36 −0.66]/51.7 deg
V18		$[1\ \ 1\ \ 0]_\gamma//$ $[-1\ \ 1\ \ -1]_{\alpha'}$	[−0.30 −0.63 −0.72]/ 47.1 deg
V19	$(11-1)_\gamma//$ $(011)_{\alpha'}$	$[-1\ \ 1\ \ 0]_\gamma//$ $[-1\ \ -1\ \ 1]_{\alpha'}$	[−0.61 0.19 −0.77]/50.5 deg
V20		$[-1\ \ 1\ \ 0]_\gamma//$ $[-1\ \ 1\ \ -1]_{\alpha'}$	[−0.36 −0.60 −0.71]/ 57.2 deg
V21		$[0\ \ -1\ \ -1]_\gamma//$ $[-1\ \ -1\ \ 1]_{\alpha'}$	[0.96 0.00 −0.30]/20.6 deg
V22		$[0\ \ -1\ \ -1]_\gamma//$ $[-1\ \ 1\ \ -1]_{\alpha'}$	[−0.72 0.30 −0.63]/47.1 deg
V23		$[1\ \ 0\ \ 1]_\gamma//$ $[-1\ \ -1\ \ 1]_{\alpha'}$	[−0.74 −0.25 0.63]/57.2 deg
V24		$[1\ \ 0\ \ 1]_\gamma//$ $[-1\ \ 1\ \ -1]_{\alpha'}$	[0.91 −0.41 0.00]/21.1 deg

2. Experimental procedure

2.1. Materials and heat treatment

A commercialized medium C steel (SCM435) was used in this study. The detailed chemical composition was shown in Table 2. The specimen was austenitized at 1173 K for 15 min in a vacuum furnace, followed by water quenching to achieve fully martensitic microstructure. Subsequently, the as quenched specimen was tempered at 673 K for 30 min in a salt bath and water quenched to room temperature. The final microstructure exhibited a tempered lath martensite with carbide precipitation (supplementary material, Fig. S2). The average PAGS was approximately 15 µm. The specimen exhibited a yield strength of 1416 MPa, a tensile strength of 1549 MPa, and a total elongation of 7%, as reported elsewhere by the co-authors [45].

Table 2

Chemical composition of SCM435 in mass%.

SCM435	C	Cr	Mn	Mo	Si	Ni	B	P	S	Fe
Mass.%	0.35	0.97	0.68	0.18	0.28	0.01	1.3ppm	68 ppm	40 ppm	Bal.

2.2. Hydrogen-induced crack preparation

The specimen was plastically deformed through U-bending with bending radius of 10 mm before hydrogen charging to induce residual stress inside the specimen. Then, hydrogen was introduced by means of cathode changing, using a 3 wt.% NaCl + 3 g/L NH_4SCN solution with a current density of 10 A/m^2 at 298 K for 24 h. The procedure was schematically illustrated in previous report [45]. The hydrogen concentration was estimated to be 1.8 mass ppm measured by thermal desorption spectrometry (TDS). As a result, multiple hydrogen-induced cracks mainly propagated along the PAGB could be obtained. Fig. 1a and b show an example microstructure of a crack propagated along the PAGB.

2.3. Microstructure characterization

The microstructure was mainly investigated by electron backscatter diffraction (EBSD) technique equipped with scanning electron microscope (SEM; JSM-7001F, JEOL). The accelerating voltage was set at 15 kV with a working distance of 15 mm. The specimen was mainly prepared by mechanical polishing to 0.06 μm colloidal silica to prevent blunting of crack propagation path caused by electrochemical polishing. In addition, electrochemical polishing was also employed when a comparison of EBSD and SEM micrographs was needed. Fig. 1c to e display the example of EBSD analysis to measure the $\theta_{\alpha'}$ and θ_γ. The major crack propagation path was PAGB, confirmed by reconstructing the orientation map of prior austenite grain (Fig. 1c$_2$, d$_2$ and e$_2$) from orientation data of martensite measured by EBSD (Fig. 1c$_1$, d$_1$ and e$_1$). The crack propagation path (black line in Fig. 1 c$_1$) was arbitrarily drawn over the orientation map of reconstructed austenite based on martensite orientation map. The orientations of prior austenite were reconstructed using software developed by co-authors [46,47]. It has been reported that the precisely measured orientation relationship between lath martensite and austenite is slightly deviates from the exact KS OR (1.6° and 2.8° from the close packed plane and direction, respectively) [46]. Therefore, to achieve better reconstruction quality, a more precisely determined orientation relationship was used for the reconstruction (120.1°, 8.8°, 195.6° in Euler angle). Subsequently, $\theta_{\alpha'}$ and θ_γ were measured across PAGBs from both non-fractured PAGBs (Fig. 1d) and fractured PAGBs

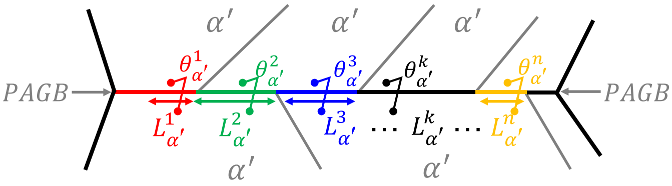

Fig. 2. Schematic illustration of low misorientation martensite segment fraction (LMSF).

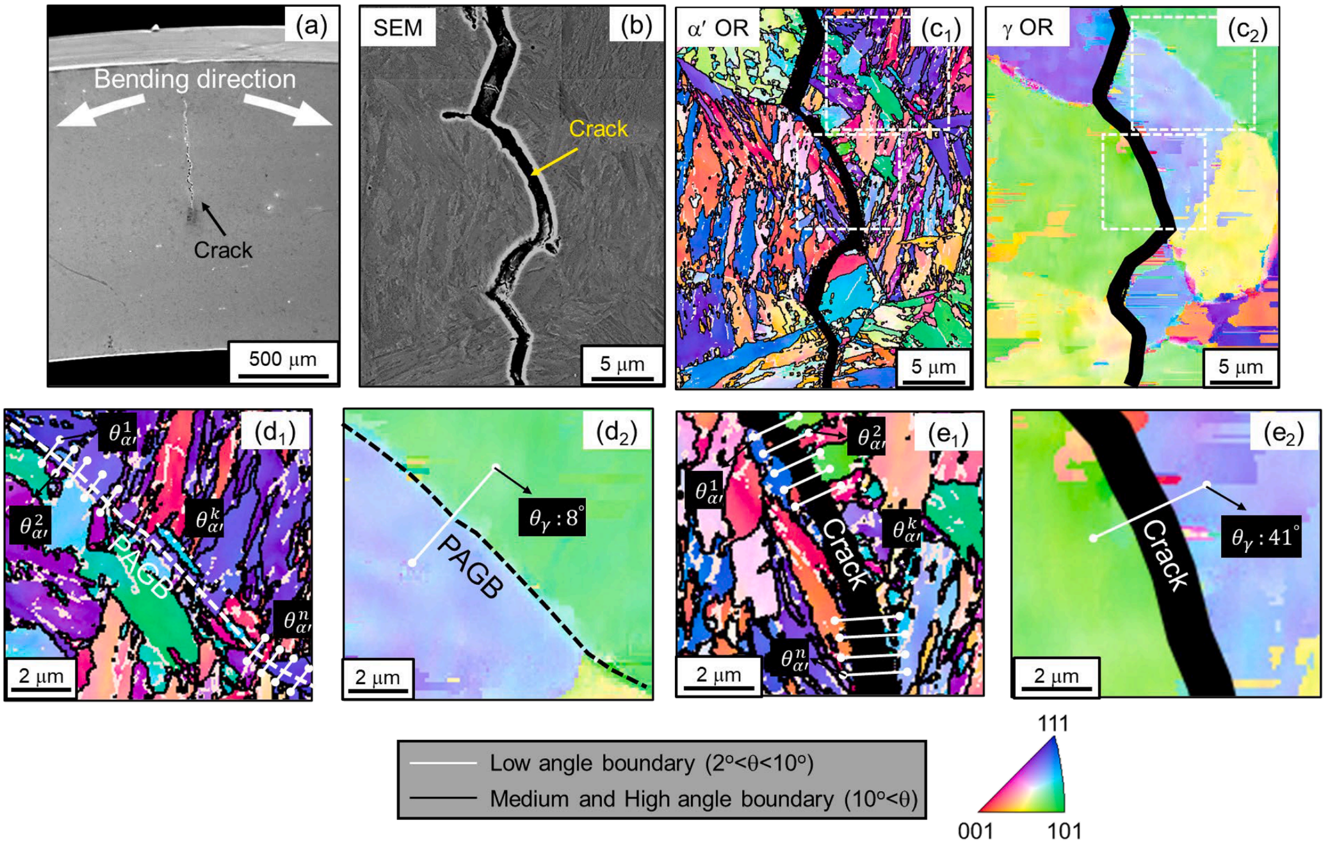

Fig. 1. Observation of a hydrogen-induced crack. (a) Low magnification SEM micrograph, (b) High magnification SEM micrograph, (c$_1$) Martensite orientation map, (c$_2$) Reconstructed austenite orientation map, (d$_1$) Martensite orientation map of non-fractured PAGB, (d$_2$) Reconstructed austenite orientation map of non-fractured PAGB, (e$_1$) Martensite orientation map of fractured PAGB, (e$_2$) Reconstructed austenite orientation map of fractured PAGB.

(Fig. 1e). The total number of PAGBs (non-fractured + fractured) was 286, with total length of 2.3 mm. It should be noted that Σ3 boundary was not included in the statistics.

Three-dimensional atom probe tomography (3D-APT: LEAP-4000HR, CAMECA) was conducted to investigate the element segregation at PAGBs depending on θ_γ. Several needle shaped tips for 3D-APT analysis were fabricated by focused ion beam (FIB) method after confirming PAGB using EBSD analysis. The analysis conditions for 3D-APT are as follows; pulse fraction: 0.2, pulse rate: 200,000 Hz, specimen temperature: 90 K.

2.4. *Evaluation of PAGB coherency*

It has been reported that low misorientation martensite segments can accommodate crack tip stress through plastic deformation and suppress the crack propagation [41]. The effectiveness of suppressing crack propagation is not determined solely by the presence of low misorientation martensite segments, but more specifically by the fraction of PAGB length occupied by these segments. Therefore, a new parameter called "Low Misorientation martensite Segment Fraction (LMSF)" is proposed here (Fig. 2). The LMSF is defined as the fraction occupied by the low misorientation martensite segments whose $\theta_{\alpha'}$ is less than 10° and is estimated by the following equation.

$$(\mathrm{LMSF}) = \frac{\sum_{k=1}^{n} L_{\alpha'}^{k}\left(\theta_{\alpha'}^{k} < 10^\circ\right)}{\sum_{k=1}^{n} L_{\alpha'}^{k}} \tag{1}$$

Here, $L_{\alpha'}^{k}$ represents the length of *k*th martensite segment in a given PAGB, and $L_{\alpha'}^{k}\left(\theta_{\alpha'}^{k} < 10^\circ\right)$ represents the length of *k*th martensite segments whose $\theta_{\alpha'}$ is less than 10°.

3. Results

3.1. *Comparison of $\theta_{\alpha'}$ and θ_γ distributions between total PAGBs and fractured PAGBs*

Fig. 3a shows length fraction of $\theta_{\alpha'}$ in total PAGBs and fractured PAGBs. It demonstrates that the LMSF of fractured PAGB is lower than that of total PAGBs. This result provides statistical support for the previous studies indicating that low misorientation martensite segments prevent PAGB cracking [8,41,48].

Fig. 3b indicates length fraction of θ_γ in total PAGBs and fractured PAGBs. PAGBs were categorized into L-PAGB ($\theta_\gamma < 10^\circ$), M-PAGB ($10^\circ < \theta_\gamma < 45^\circ$), and H-PAGB ($\theta_\gamma > 45^\circ$). A distinctive observation is that the length fraction of L-PAGB in fractured PAGBs is lower than that in total PAGBs, suggesting that cracks could hardly propagate along the L-PAGB. The length fraction of M-PAGB, especially for θ_γ ranging from 20° to 45°, is higher in fractured PAGBs than in total PAGBs, indicating that M-PAGB is vulnerable to hydrogen-induced cracking. For H-PAGB, there is no significant difference in length fraction between total PAGBs and fractured PAGBs.

The reason why hydrogen-induced cracks typically initiate at PAGBs is presumably related to the high hydrogen concentration. Many previous studies qualitatively demonstrated that hydrogen atoms are preferentially localized at PAGBs by hydrogen microprint technique [4]. As explained, PAGB is not a homogenous grain boundary but consists of several martensite boundary segments with high misorientation. In general, the amount of impurity segregation increases with increasing misorientation angle [33-35]. Although we cannot directly evaluate hydrogen concentration at the boundary, it can be speculated that more hydrogen atoms are segregated in high angle grain boundaries compared to low angle grain boundaries, leading to boundary decohesion (HEDE mechanism). However, the reason why PAGB is particularly more vulnerable to hydrogen-induced cracking than other high angle grain boundaries of martensitic microstructure (packet, block boundaries) is still controversial. This is presumably related to the segregation of impurities such as P, S, and Sn occurs during austenitizing [26]. Their influence on hydrogen-induced cracking will be addressed in another paper.

3.2. *Relation between $\theta_{\alpha'}$ and θ_γ*

Fig. 4a shows the relation between $\theta_{\alpha'}$ and θ_γ in total PAGBs and the corresponding heat map. Two distinctive features were observed: (1) L-PAGB can hardly achieve martensite segments with a range of $\theta_{\alpha'}$ approximately between 20° to 40°, and (2) M-PAGB, particularly θ_γ between 20° to 45°, can hardly achieve low misorientation martensite segments ($\theta_{\alpha'} < 10^\circ$). The first feature (1) can be explained by examining the inter-variant misorientation distribution of the 24 KS variants (Table 1). The inter-variant misorientations were plotted with filled circles at θ_γ of 0°. Misorientation ranging from 22° to 47° cannot be achieved in the KS OR inter-variant misorientation. Therefore, when θ_γ is low enough to be regarded as almost a single grain, it shows a similar trend to the inter-variant misorientation distribution, and the impact

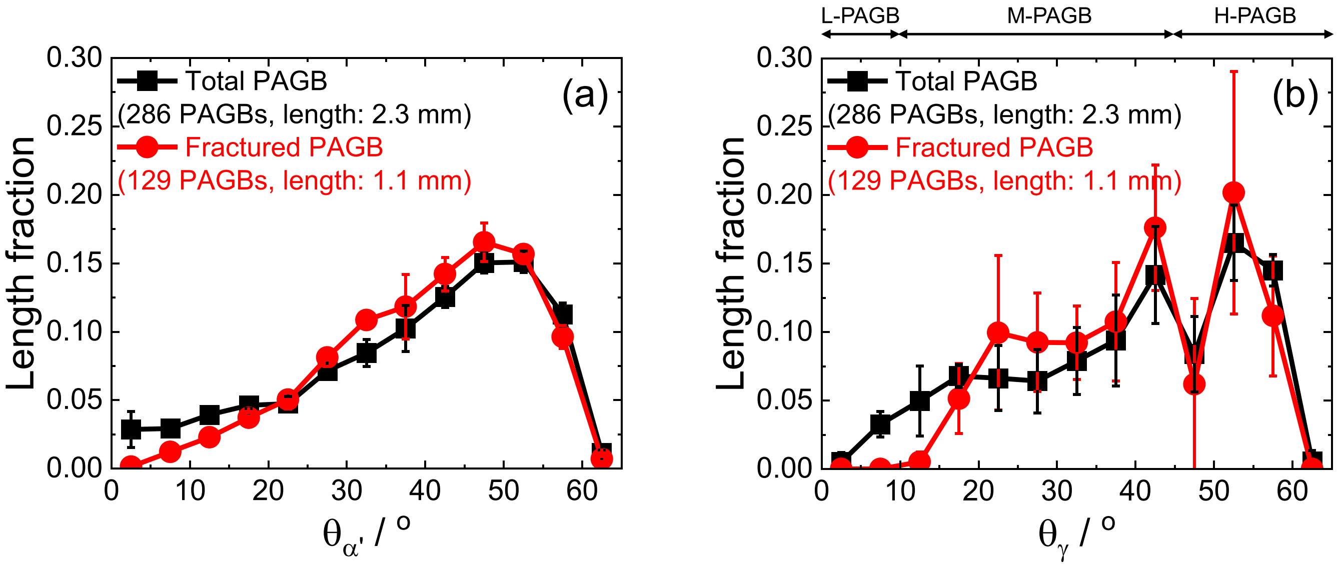

Fig. 3. (a) Comparison length fraction against $\theta_{\alpha'}$ between fractured PAGB and total PAGB (b) Comparison of length fraction against θ_γ between fractured PAGB and total PAGB.

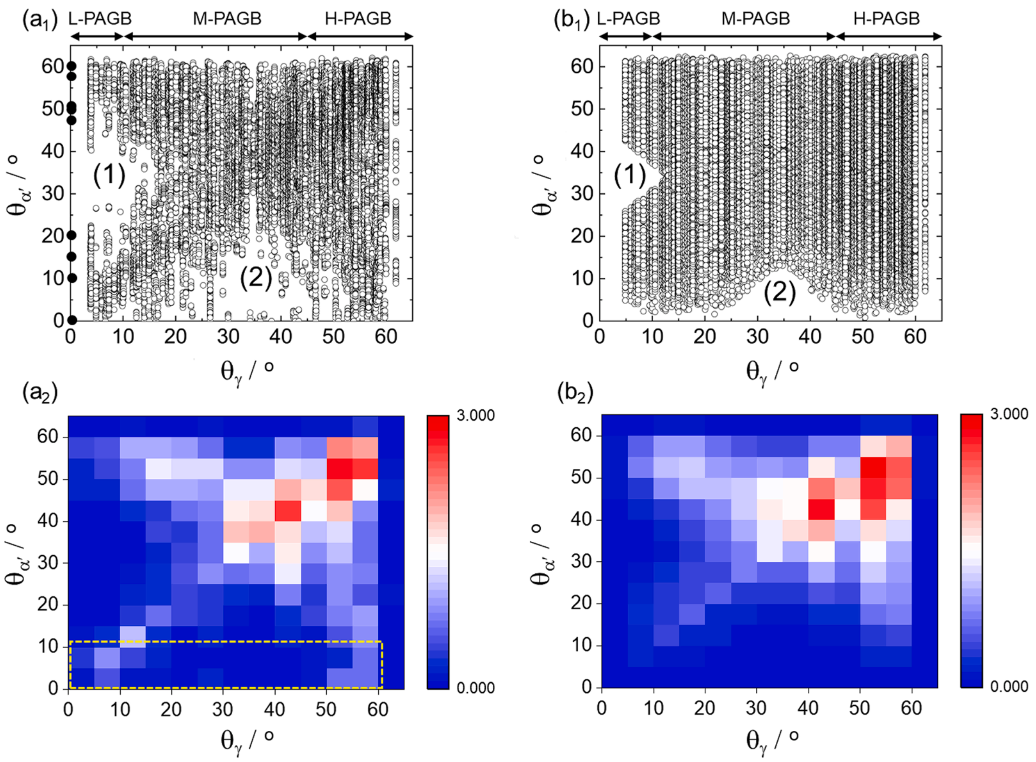

Fig. 4. Scatter diagrams and heat maps showing relation between $\theta_{\alpha'}$ and θ_γ in total PAGB (a) Measurement, (b) Calculation based on γ orientation assuming no variant selection.

becomes blurred with increasing θ_γ. The second feature (2) can be also explained by considering inter-variant misorientation. Since the inter-variant misorientation cannot exhibit a range from 22° to 47°, it is difficult to obtain low misorientation martensite segments if the θ_γ is between 22° to 47° due to symmetric feature of KS OR between FCC and BCC. This is the reason why the length fraction of M-PAGB (especially for $20° < \theta_\gamma < 45°$) was higher in fractured PAGBs than in total PAGBs.

To analyze the effects of variant selection on the relation between $\theta_{\alpha'}$ and θ_γ, calculation was conducted based on an equal formation of all the possible 24 KS variants from reconstructed austenite orientation data as shown in Fig. 4b. Although the distribution shape and distinctive features ((1) and (2)) found in the measurement were quite well reproduced by the calculation, the heat maps show slight differences between them (Fig. 4a$_2$ and b$_2$). The most notable difference is that the fraction of low misorientation martensite segment ($\theta_{\alpha'} < 10°$), crucial for suppressing PAGB cracking, is more preferentially formed in the measurement than

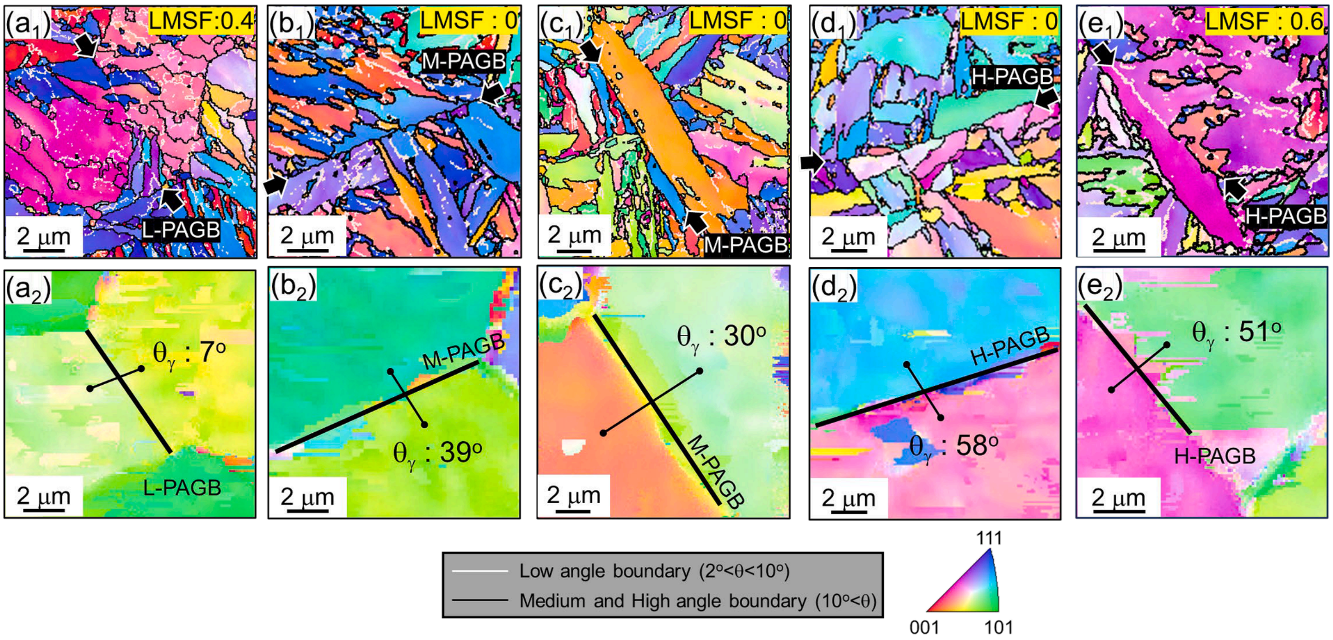

Fig. 5. Microstructure adjacent to PAGB with various θ_γ. Martensite orientation map adjacent to l-PAGB (a$_1$), M-PAGB (b$_1$ and c$_1$), and L-PAGB (d$_1$ and e$_1$). Reconstructed austenite orientation map adjacent to l-PAGB (a$_2$), M-PAGB (b$_2$ and c$_2$), and L-PAGB (d$_2$ and e$_2$).

in the calculation as highlighted in yellow dotted rectangle. This suggests that specific martensite variants are preferentially formed at PAGB.

3.3. *Microstructure adjacent to PAGB and low misorientation martensite segment fraction (LMSF)*

Fig. 5 shows representative EBSD orientation maps of martensite and reconstructed austenite adjacent to PAGB depending on the θ_γ. Fig. 5a, Fig. 5b and c, Fig. 5d and e correspond to L-PAGB ($\theta_\gamma < 10°$), M-PAGB ($10° < \theta_\gamma < 45°$), and H-PAGB ($\theta_\gamma > 45°$), respectively. The martensite boundary misorientation was highlighted by black ($> 10°$) or white ($< 10°$) lines depending on the misorientation angle. PAGB was confirmed by the reconstructed austenite orientation map and indicated by black arrows (Figs. 5a_2 to e_2). Two cases of variant features were observed; Case1: multiple fine variants dominant on both side of PAGB (Figs. 5a_1, b_1, and d_1) and Case2: a coarse variant dominant at least one side of PAGB (Figs g. 5c_1 and e_1). The former case (Case1) is the commonly observed feature for most of PAGBs, but the latter case (Case2) is seldom and observed only in M-PAGB and H-PAGB. The LMSF was found to be highly influenced by θ_γ and variant features. L-PAGB exhibits relatively high LMSF, although formation of multiple fine variants (Case1) is one of the factors deteriorating LMSF (Fig. 5a). As explained earlier, M-PAGB generally exhibits low LMSF due to intrinsic inter-variant misorientation of KS OR independent of variant feature. However, the variant feature becomes crucially related to LMSF in H-PAGB. H-PAGB exhibits relatively low LMSF when variant feature is Case1 (Fig. 5d), while relatively high LMSF when variant feature is Case2 (Fig. 5e) unlike L-PAGB where high LMSF is related to Case1 (Fig. 5a).

This finding is supported by the statistical data as shown in Fig. 6. Fig. 6a shows the relation between LMSF and θ_γ in total PAGBs. The empty and filled circles indicate variant feature Case1 and Case2, respectively. Most of L-PAGBs show high LMSF (> 0.3), and the variant feature was Case1. Most of M-PAGBs show low LMSF (< 0.3) independent of variant feature. H-PAGBs could exhibit a wide range of LMSF from 0 to 1.0. It is clear that H-PAGBs whose variant feature is Case2 tend to have a higher LMSF. Fig. 6b shows the statistical data for fractured PAGBs. Compared with total PAGBs (Fig. 6a), it was found that a crack can hardly propagate PAGB whose LMSF is over 0.3, which suggests that LMSF is an appropriate parameter determining cracking resistance of PAGB. Then, LMSF of 0.3 could be regarded as a safety criterion determining cracking resistance of PAGB. Fig. 6c shows that the calculated LMSF with reconstructed austenite orientation data by assuming all the 24 KS variants were equally formed. The overall LMSF is much smaller in the calculation than in the measurement, implying that martensite segment at actual PAGB tends to be low misorientation due to variant selection in nucleation at PAGB.

4. Discussion

In the result section, it has been demonstrated that L-PAGB ($\theta_\gamma < 10°$) exhibits greater resistance to hydrogen-induced PAGB cracking compared to M-PAGB ($10° < \theta_\gamma < 45°$) and L-PAGB ($45° < \theta_\gamma$). One contributing factor is that L-PAGB always exhibits a high LMSF (Fig. 6a). Another potential factor influencing crack propagation resistance is PAGB segregation. It has been reported that the amount of segregation is influenced by boundary misorientation [34]. This implies that the observed resistance of L-PAGB to cracking might be attributed to a lower amount of segregation of grain boundary weakening elements. Therefore, a quantitative analysis of the PAGB segregation depending on θ_γ was performed.

4.1. *Influence of θ_γ on PAGB segregation and cohesion*

4.1.1. *PAGB segregation analyzed by 3D-APT*

The amount of PAGB segregation was quantitatively analyzed with 3D-APT analysis at PAGB whose θ_γ were 7°, 15°, and 43°. Multiple 3D-APT tips were fabricated in the same PAGB after confirming its θ_γ (Fig. 7a). The number of successfully analyzed tips was 2, 1, and 4 for PAGBs with θ_γ of 7°, 15°, and 43°, respectively. Fig. 7b shows an example of the 3D-APT results from a PAGB with θ_γ of 15° (other results are available in the supplementary material, Fig. S3). The segregation of C, B, P, and Mo was characterized at the PAGB (Fig. 7b_1). Fig. 7b_2 shows representative examples of composition profiles across PAGB. Segregation of C was the most remarkable because the nominal composition of C is much higher than other elements. The amount of element segregation at PAGB was evaluated based on an interfacial excess [49], and the average values were estimated. Using the average interfacial excesses, the atomic percentage (at.%) of the segregation was estimated by assuming the site density per unit area of grain boundary, which was 48 sites/nm^2 [33,50]. Fig. 8 displays the result of the average segregation amount at PAGB depending on θ_γ. The amount of segregation is higher in M-PAGB than that in L-PAGB for most of the elements, which implies that θ_γ plays a dominant role in PAGB segregation. This is reasonable because all the elements can be segregated to austenite grain boundary during austenitizing, influenced by θ_γ, while only limited elements with high diffusivity, such as C, can be segregated during tempering, influenced by $\theta_{\alpha'}$. To confirm it, diffusion distance was estimated during austenitizing and tempering by the following equation. The diffusivity data were referred from [51,52] (C), [53,54] (B), and [55] (P and Mo)

$$\text{Diffusion distance} = \sqrt{2Dt} \tag{2}$$

$$D = D_0 \exp\left(-\frac{Q}{RT}\right) \tag{3}$$

Here, D is diffusivity, D_0 is a pre-exponential coefficient, Q is activation energy, R is a gas constant, and T is temperature in Kelvin.

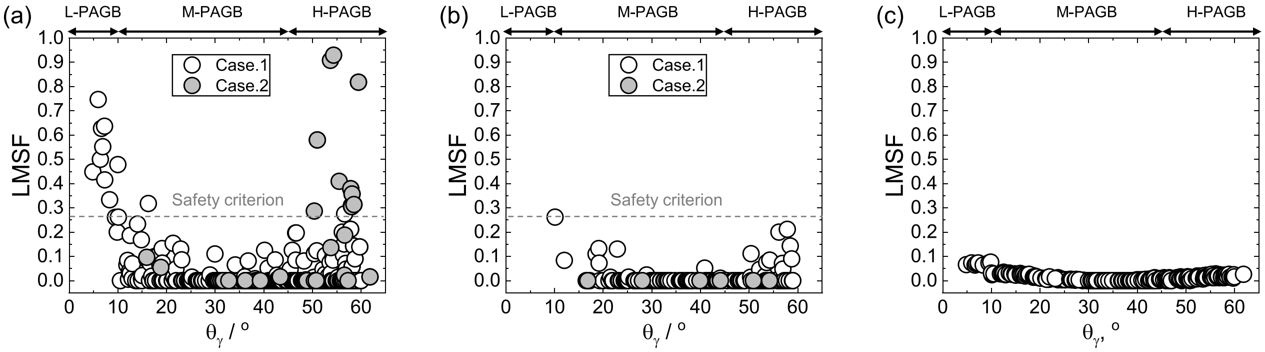

Fig. 6. Relation between LMSF and θ_γ (a) Measurement in total PAGB, (b) Measurement in fractured PAGB, and (c) Calculation based on random formation of 24 KS martensite variant from orientation data of austenite in total PAGB.

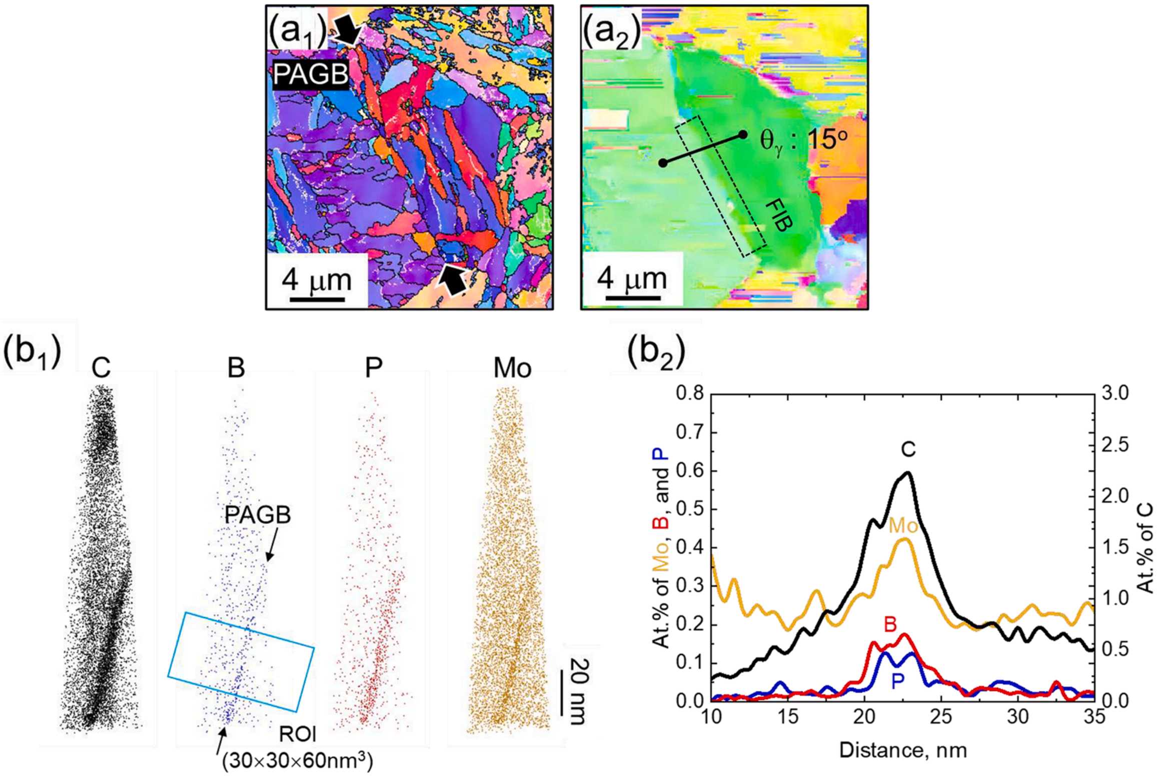

Fig. 7. Representative result of 3D-APT analysis (a_1) Orientation map of martensite and (a_2) reconstructed austenite where 3D-APT tips were fabricated (b_1) Three-dimensional atom maps of C, B, P, and Mo (b_2) Line profile across PAGB indicated by the region of interest (ROI, 30 × 30 × 60 nm^3) in (b_1).

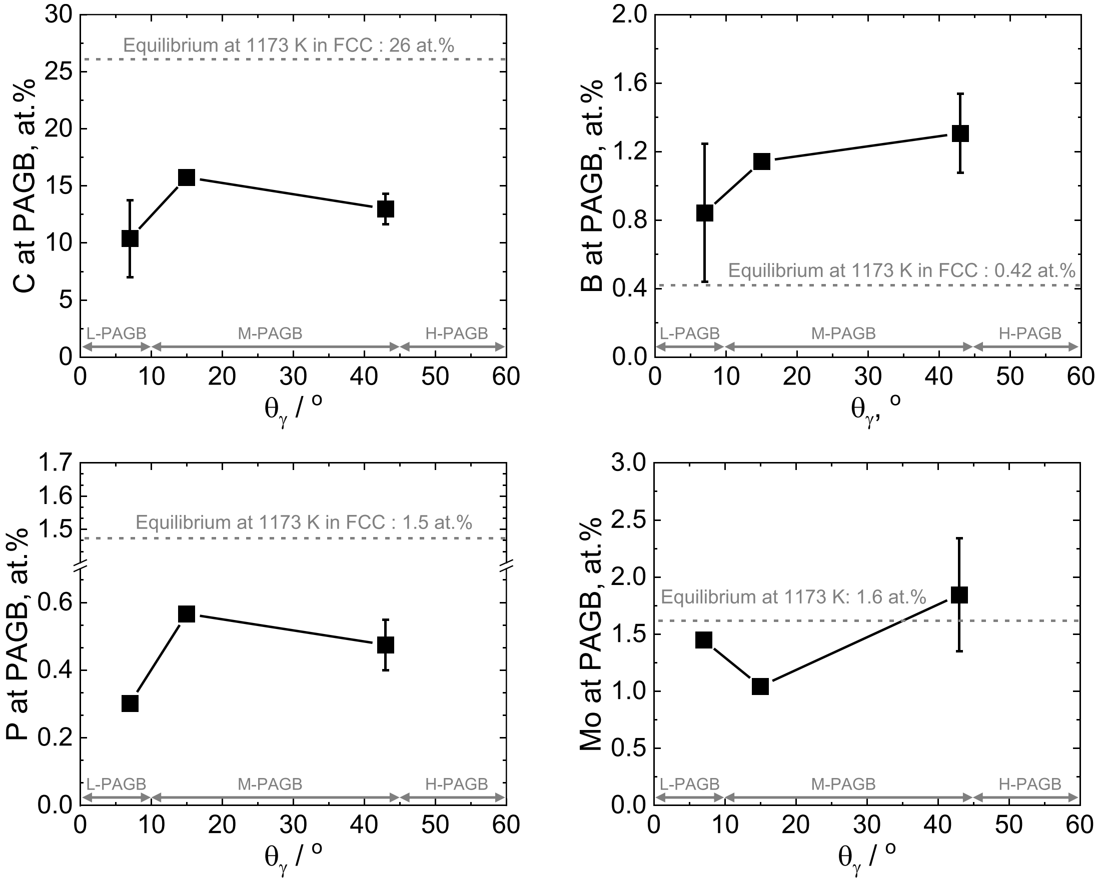

Fig. 8. Average atomic fraction in PAGB depending on θ_γ. (a) C, (b) B, (c) P, and (d) Mo.

The diffusion distances of C, B, P, and Mo were approximately to be 1.2×10^4 μm, 1.6×10^2 μm, 1.0 μm, and 3.7×10^{-1} μm, respectively during austenitizing (1173 K for 15 min), and 4.6×10^1 μm, 3.8×10^{-3} μm, 1.2×10^{-3} μm, and 1.0×10^{-3} μm, respectively during tempering (673 K for 30 min). Considering the grain boundary thickness (approximately 6×10^{-4} μm [50]), all the elements can be segregated during austenitizing, while only C can be practically segregated during tempering, which is why the result shows high θ_γ dependency.

Since the amount of segregation was mainly determined during austenitizing, it is reasonable to compare the result with the equilibrium segregation at 1173 K. Horizontal dotted lines in Fig. 8 indicate the equilibrium amount of segregation at 1173 K calculated by the following McLean's equation.

$$\frac{X_{GB}}{1 - X_{GB}} = \frac{X_B}{1 - X_B} \exp\left(\frac{-\Delta G}{RT}\right) \tag{4}$$

Here, X_{GB} is an atomic fraction of the segregant at grain boundary, X_B is a bulk composition, -ΔG is a segregation energy, R is a gas constant, and T is a temperature in Kelvin.

The utilized segregation energies of the C, B, P, and Mo were −30 kJ/mol [56], −63 kJ/mol [57], −47 kJ/mol [56], and −27 kJ/mol [50], respectively. The amount of C segregation was less than the equilibrium value because C will be consumed by cementite precipitation during tempering.

It should be noted that not only θ_γ and but also $\theta_{\alpha'}$ influence on C segregation. Although $\theta_{\alpha'}$ was not measured at the APT tips, we already know that about half of the L-PAGB (θ_γ: 7°) is low $\theta_{\alpha'}$ segments while M-PAGB (θ_γ: 43°) mostly consists of high $\theta_{\alpha'}$ segments (Fig. 6). Therefore, high fraction of low $\theta_{\alpha'}$ segment results in lower average C segregation amount in L-PAGB than that in other PAGBs. For B segregation, the measurements are above the equilibrium value, which can be explained by non-equilibrium segregation mechanism. In the non-equilibrium segregation mechanism, a vacancy and B complex, formed due to attractive interaction, results in additional segregation of B during cooling [33]. The amount of P segregation is much lower than the equilibrium value, mainly due to repulsive interactions with C and B during austenization [21,31,58]. Mo does not show the clear dependency on θ_γ, but the measurements corresponded well to the equilibrium value.

4.1.2. Influence of PAGB segregation on PAGB cohesion

The 3D-APT results demonstrated that the amount of segregation increases with increasing θ_γ. This implies that the finding of this study, where L-PAGB is more resistant to cracking than M-PAGB and H-PAGB, might be due to the less segregation of harmful elements such as P. To confirm it, the influence of these elements on grain boundary cohesion was evaluated. Among the segregated alloy elements in this study, P is known to be grain boundary weakening elements, while C, B, and Mo are known to be grain boundary strengthening elements [21,59-61]. Since it is challenging to directly measure grain boundary cohesion, qualitative comparison was made by comparing their influences on ductile to brittle transition temperature (DBTT) using reported empirical relations by assuming the effects are similar regardless of misorientation. The change in DBTT (ΔDBTT) of ferritic steel with the boundary segregations of C, B and P were reported to be −10 K/at.%, −20 K /at.% and 7 K /at.%, respectively [21]. The effect of Mo could not be considered due to a lack of data. Using these empirical relations, ΔDBTT was evaluated depending on θ_γ and summarized in Table 3. The ΔDBTT is more remarkable in M-PAGBs than in L-PAGB and most of contribution is originated from C segregation. This implies that increasing θ_γ is beneficial to crack resistance in terms of PAGB segregation, which contradicts the finding that L-PAGB is more resistant to cracking. Not considering the effect of Mo does not influence the conclusion because the amount of Mo, grain boundary strengthening element, is more segregated in M-PAGB (θ_γ: 43°) than L-PAGB. Those results suggest that PAGB segregation is not the major factor determining the crack resistance of PAGB in this study.

Table 3
Contribution of PAGB segregation to ΔDBTT depending on θ_γ.

ΔDBTT,	L-PAGB (θ_γ: 7°)	M-PAGB1 (θ_γ: 15°)	M-PAGB2 (θ_γ: 43°)
C (−10 K/at.%)	−97	−158	−132
B (−20 K/at.%)	−15	−22	−26
P (+7 K/at.%)	+2	+4	+3
Mo (no data)	–	–	–
Total	−110	−176	−155

4.2. Influence of θ_γ on low misorientation martensite segment fraction (LMSF) and requirements for high LMSF

The above analyses implies that what plays a crucial role in preventing PAGB cracking is not grain boundary segregation, but the intrinsic coherency, which is represented as LMSF in this study. Therefore, it is important to investigate the requirements for the PAGB to exhibit high LMSF. For PAGB to exhibit a high LMSF, it is required to be either L-PAGB ($\theta_\gamma < 10°$) or H-PAGB ($\theta_\gamma > 45°$) as shown in Fig.6. Unlike L-PAGBs, which generally exhibit a high LMSF independent of variant features, H-PAGB exhibits high LMSF only when the variant feature is Case2 (few coarse variants). Thus, it is necessary to investigate the condition where the coarse variant can be formed at H-PAGB.

The variant formation of martensite/bainite is highly influenced by the accommodation of transformation strain [62,63]. The strain can be accommodated either by plastic deformation of adjacent untransformed austenite or formation of another martensite variant. The former occurs when the austenite is soft enough to be plastically deformed, which is the case with low C concentration or a high transformation temperature. On the other hand, the latter occurs in the opposite situation (high C and low transformation temperature). The latter case leads to refinement of martensite/bainite variant and is the main mechanism for microstructure change of martensite/bainite depending on C concentration and transformation temperature [62,64]. Therefore, it is expected that the coarse martensite variant is likely to be nucleated in the initial stage of the martensitic transformation when the transformation temperature is relatively high, and influence of another variant is negligible. In connection to this, Morsdorf et al. also insisted that the coarse martensite variant is nucleated from the PAGB in the early stage of the transformation based on the comprehensive investigation on C segregation and nano-hardness depending on size of the martensite variant [65]. To confirm that the coarse variant predominantly formed in the initial stage of transformation, an interrupted quenching treatment was employed [66]. An interrupt quenching treatment allows initially nucleated martensite to be tempered during the interrupt holding, which makes it possible to differentiate between initially nucleated martensite (tempered martensite) from other martensite (fresh martensite). The detail explanation of the interrupted quenching treatment is explained in supplementary materials (Figs. S4 and S5). Fig. 9 shows microstructure and LMSF in the interrupted quenched specimen. A similar trend to Fig. 6a was observed: L-PAGB exhibits a high LMSF, M-PAGB hardly exhibits a high LMSF, and H-PAGB exhibits a wide range of LMSF. The initially nucleated PAGBs are indicated by filled symbols and the number of initially nucleated PAGB analyzed (filled symbols) was 18. It should be noted that the Σ3 boundary was not included in the statistics, despite being a strong nucleation site for martensite [44]. It was observed that the initially nucleated PAGBs were mainly M-PAGB and H-PAGB, implying high nucleation potency presumably due to their high grain boundary energies. On the other hand, tempered martensite was hardly observed on L-PAGB, suggesting low nucleation potency. The size of initially nucleated martensite variant (5.8 ± 1.8 μm) was much larger than average martensite variant size (3.2 ± 1.9 μm), which is

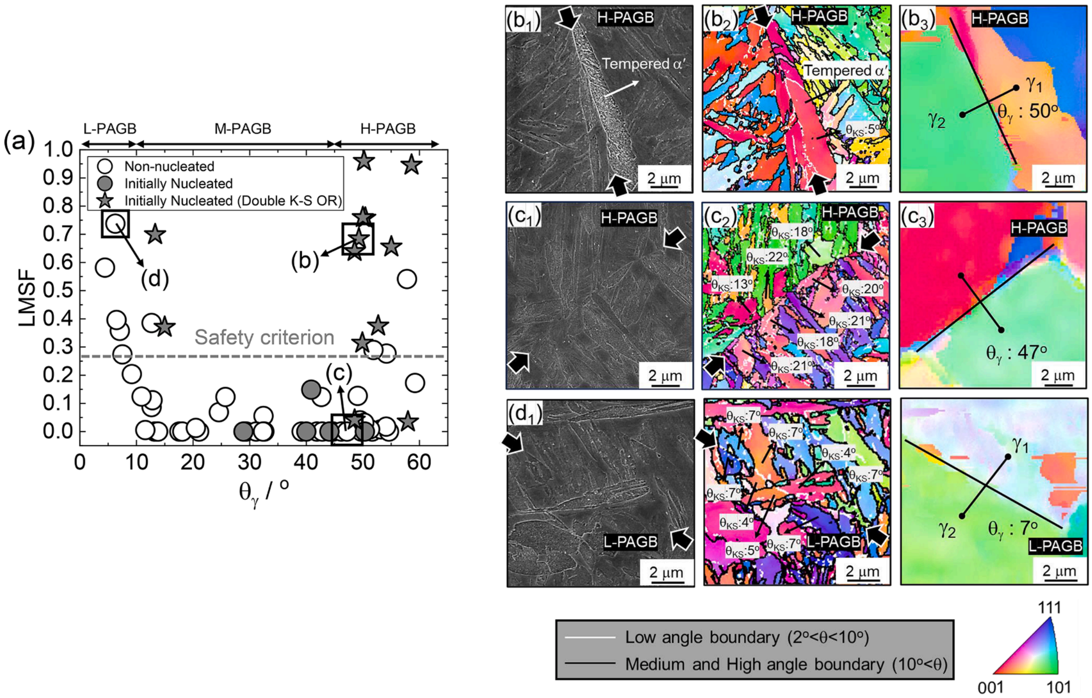

Fig. 9. (a) Relation between LMFS and θ_γ in interrupted quenching treated specimen. Initially nucleated and non-nucleated PAGBs are denoted by filled symbols (circle for non-KS and star for double KS) and open symbols, respectively. (b) Microstructure adjacent to initially nucleated H-PAGB, exhibiting high LMSF. (c) Microstructure adjacent to non-nucleated H-PAGB, exhibiting low LMSF. (d) Microstructure adjacent to non-nucleated L-PAGB, exhibiting high LMSF.

consistent with a previous study proposing that coarse martensite variants are formed at the initial stage of the transformation [65]. An interesting finding was that most of H-PAGBs exhibiting high LMSF belong to initially nucleated PAGBs. Fig. 9b shows the microstructure adjacent to initially nucleated H-PAGB, exhibiting high LMSF. A coarse martensite variant, characterized by the presence of carbide, was nucleated at H-PAGB. The variant feature of the initially nucleated H-PAGB is Case2 (few coarse variants). On the other hand, non-nucleated H-PAGB (non-tempered martensite) generally shows Case1 variant feature while exhibiting extremely low LMSF (Fig. 9c). This finding indicates that the nucleation event is favorable to exhibit high LMSF in H-PAGB.

When it comes to grain boundary nucleation of bainite/martensite, double KS OR should be investigated since it is a necessary condition to exhibit high LMSF. To determine whether the nucleated martensite satisfies the double KS OR or not, the deviation angle of KS OR from the opposite grain sharing the boundary (θ_{KS}) was evaluated, and the threshold θ_{KS} of double KS OR was determined to be below 10° ($\theta_{KS} <$ 10°). Fig. 10 shows the result of measured θ_{KS} of the 18 PAGBs where martensite is initially nucleated. PAGB numbers were labeled in order of increasing θ_γ. Open circles indicate all the possible 48 θ_{KS} (24 from each austenite grain) and filled circles indicate the θ_{KS} of martensite nucleated. About 72 % of the initially nucleated PAGBs satisfied double KS OR. The value is much greater than the probability that an arbitrary grain satisfies the double KS OR (about 11%), which implies that interfacial energy minimization induced by coherent interface of grains with KS OR is one of the key mechanisms for variant selection in grain boundary nucleation of medium C martensite. The probability that an arbitrary grain satisfies the double KS OR depending on threshold angle (10° in this study) is also available in supplementary materials (Fig. S6). This observation aligns with previous studies on variant selection of bainite whose C and transformation temperature are similar [43].

The result in Fig. 9a clearly shows that PAGB tends to exhibit LMSF higher than 0.3 (safety criterion) when the initially nucleated martensite variant satisfies the double KS OR. After the martensite nucleation at the grain boundary, what determines the $\theta_{\alpha'}$ is orientation of subsequent martensite variant across the austenite grain boundary. The formation of subsequent martensite is stimulated by the initially nucleated martensite and certain variant will be preferentially selected. In this case also, interfacial energy minimization could play a role, favoring the formation of a martensite variant whose orientation is almost identical to the initially nucleated martensite variant. This explains why nucleated PAGBs satisfying the double KS OR exhibit high LMSF. It should be also noted that other mechanisms, such as grain boundary elimination and strain accommodation, may also play a role. These mechanisms are presumed to be effective for PAGBs that cannot satisfy the double KS OR, such as PAGB3, PAGB4, and PAGB5 in Fig. 10. A more in-depth analysis of variant selection for subsequent martensite, stimulated by initially nucleated martensite, is beyond the scope of this study and will be addressed in a separate paper.

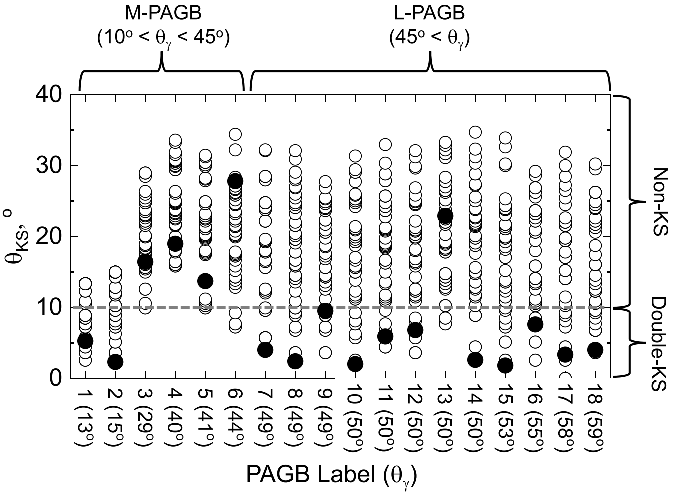

Fig. 10. Comparison between measured θ_{KS} (filled symbols) and possible 48 θ_{KS} (open symbols) of initially nucleated 18 PAGBs.

The formation of a martensite variant that satisfies double KS OR is a crucial requirement for exhibiting high LMSF. This is generally achieved by the grain boundary nucleation at an initial stage of martensitic transformation. When an H-PAGB serves as a stopping site rather than a nucleation site, where the growth of a martensite variant nucleated elsewhere is halted, achieving the double KS OR becomes difficult since it is just a random selection of the variant at the stopping H-PAGB. Fig. 9c shows microstructure of H-PAGB without tempered martensite after interrupted quenching treatment, meaning non-nucleated PAGB. Since the H-PAGB was not the initially nucleated PAGB, fine multiple variants holding non-KS OR ($\theta_{KS} > 10°$) were formed. Thereby, non-nucleated PAGB usually shows lower LMSF, making it vulnerable to hydrogen-induced cracking. In contrast, L-PAGB generally exhibits high LMSF, despite not being preferential nucleation site as shown in Fig. 9d. This is because all the variants adjacent L-PAGB always satisfy double KS OR owing to low θ_γ. Any martensite variants nucleated from elsewhere and stops at L-PAGB always satisfy double KS OR. This leads to the formation of similar orientation martensite across the L-PAGB to minimize interfacial energy, resulting in high LMSF. Additional characteristics of martensite microstructure at L-PAGB is the clear continuity of martensite variant pairs across the L-PAGB as shown in Figs. 5a and 9d. Growth of martensite could be hindered at L-PAGB with misorientations of several degrees. This inhibition leads to the nucleation of new martensite variants at the boundary due to shape deformation. To elucidate the effect of shape deformation, the direction of transformation strain and habit plane of these martensite variants were investigated. Fig. 11 shows the microstructure adjacent to L-PAGB (Fig. 5a magnified), where four pairs of variants across the L-PAGB with nearly the identical orientation were identified. The directions of transformation shape strain and habit plane of these variants were determined by phenomenological theory (PTMC) based on double lattice invariant shear deformation (LID) model. The details of the calculation are present in the Appendix. The directions of transformation strain and habit plane of all variant pairs across the L-PAGB were almost identical. These results support the hypothesis that autocatalytic nucleation of the martensite due to shape deformation could explain the formation of those martensite variant pairs at the L-PAGB, contributing to the high LMSF.

The influence of θ_γ on microstructure evolution at PAGB was schematically illustrated in Fig. 12. A dotted line indicates low angle grain boundary ($\theta_\gamma < 10°$), and solid lines indicate medium and high angle grain boundaries ($\theta_\gamma > 10°$). In the initial stage of martensitic transformation, martensite preferentially nucleates at medium and high angle austenite grain boundaries. The nucleated martensite can be categorized into double KS ($\theta_{KS} < 10°$) and non-KS ($\theta_{KS} > 10°$). The former case is more dominant, as it minimizes interfacial energy. In situations where double KS martensite is initially nucleated at the austenite grain boundary (α'_1 and α'_2), eventually, martensite with a similar orientation to initially nucleated martensite is more likely to be formed across the austenite grain boundary, resulting in high LMSF (low $\theta_{\alpha'}$). On the other hand, for the austenite grain boundary where non-KS martensite is formed (α'_3), martensite with a similar orientation to the initially nucleated martensite cannot exist in the opposite austenite, resulting in a low LMSF (high $\theta_{\alpha'}$). This is why initial nucleation at PAGB, and double KS are crucial factors for achieving high LMSF. However, it is not necessary for L-PAGB to be the initial nucleation site to achieve high LMSF. All the martensite variants satisfy the double KS OR, allowing martensite to form with the nearly identical orientation through the L-PAGB. Therefore, high LMSF is always achieved in L-PAGB, independent of nucleation event.

5. Summary

We have investigated the hydrogen-induced crack propagation path in a medium C tempered martensitic steel, focusing on intergranular cracks along the PAGB. To analyze the misorientation characteristics of fractured PAGB, we examined $\theta_{\alpha'}$ (martensite misorientation) and θ_γ (austenite misorientation) across the fractured and total PAGBs using EBSD. The main findings of this study are as follows.

1) Cracks can hardly propagated along the PAGB with low $\theta_{\alpha'}$, more specifically PAGB with low misorientation martensite ($\theta_{\alpha'} < 10°$) segment fraction (LMSF) is over 0.3.
2) Comparison of θ_γ between fractured PAGBs and total PAGBs revealed that cracks can hardly propagated along the L-PAGBs ($\theta_\gamma < 10°$), while they preferentially propagated along M-PAGBs ($10° < \theta_\gamma < 45°$). PAGB segregation investigated by 3D-APT could not explain these results as C, a grain boundary strengthening element, is more segregated at M-PAGBs. This suggests that the intrinsic coherency of martensite ($\theta_{\alpha'}$), represented as LMSF here, is a more crucial factor suppressing PAGB cracking in this study.
3) To achieve a high LMSF, PAGB should be either L-PAGB ($\theta_\gamma < 10°$) or H-PAGB ($\theta_\gamma > 45°$). M-PAGB ($10° < \theta_\gamma < 45°$) hardly exhibits high LMSF. This is because misorientations from 10° to 45° are mostly outside the inter-variant misorientation range of KS OR, making M-PAGB the most vulnerable to PAGB cracking. While the L-PAGB consistently exhibits high LMSF, H-PAGB requires a specific condition to do so: it must serve as an initial nucleation site, and the nucleated martensite has to satisfy the double KS OR.

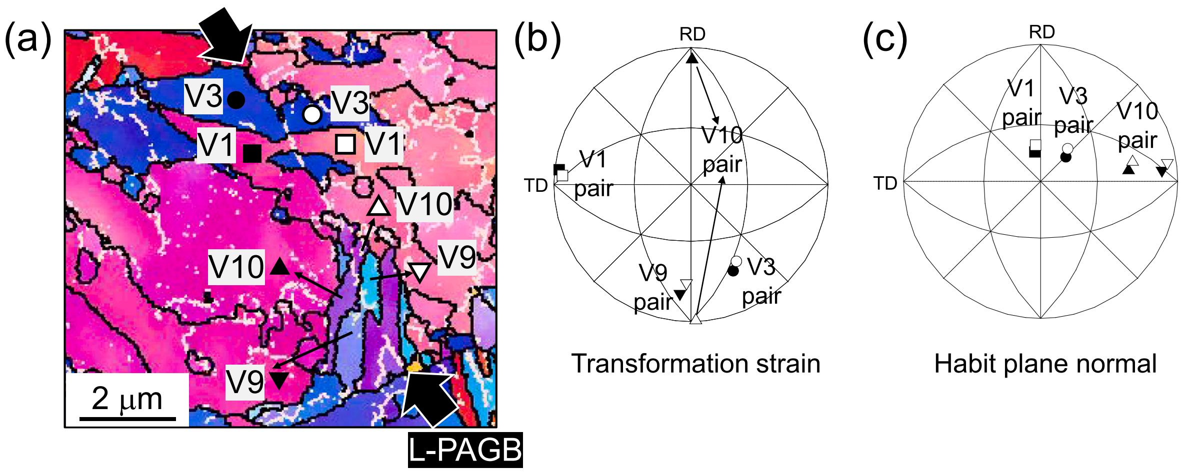

Fig. 11. (a) Martensite orientation map adjacent to L-PAGB (Fig 7a magnified). (b) Transformation strain direction of each variant pairs across the L-PAGB. (c) Habit plane normal direction of each variant pairs across the L-PAGB.

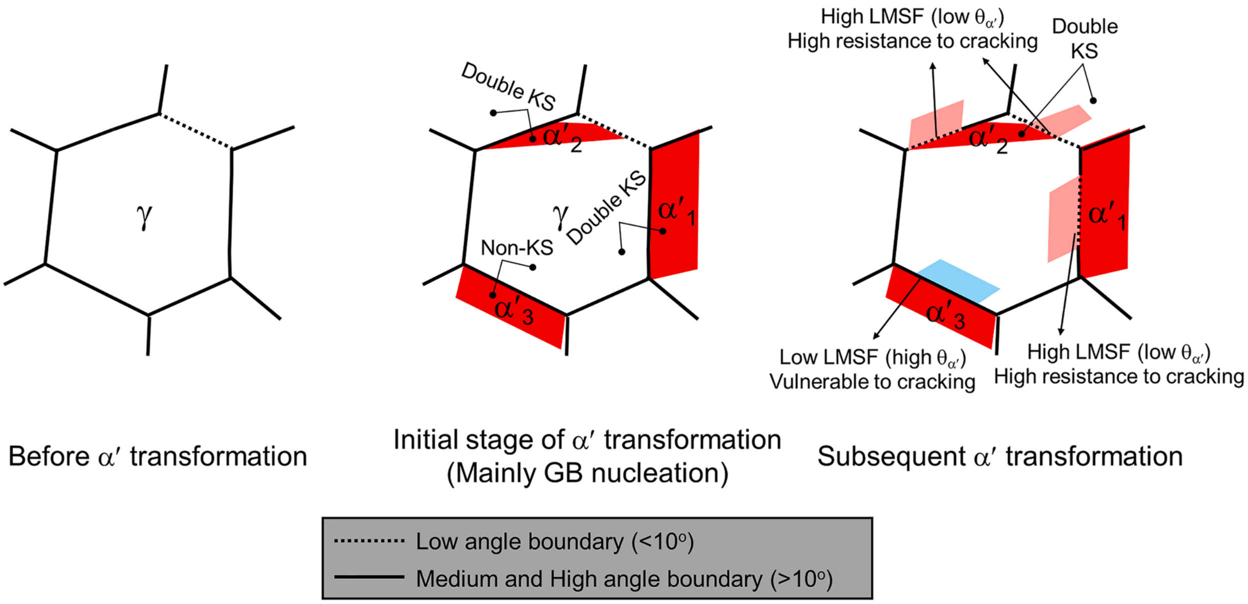

Fig. 12. Schematically illustrated microstructure evolution during martensitic transformation depending on austenite misorientation angle.

CRediT authorship contribution statement

Ji Hoon Kim: Writing – review & editing, Writing – original draft, Supervision, Methodology, Investigation, Funding acquisition, Formal analysis, Data curation, Conceptualization. **Goro Miyamoto:** Writing – review & editing, Methodology, Funding acquisition, Formal analysis, Conceptualization. **Akinobu Shibata:** Writing – review & editing. **Tomohiko Hojo:** Writing – review & editing, Resources. **Motomichi Koyama:** Writing – review & editing. **Yongjie Zhang:** Writing – review & editing. **Tadashi Furuhara:** Writing – review & editing, Funding acquisition.

Declaration of competing interest

The authors declare that they have no known competing financial interests or personal relationships that could have appeared to influence the work reported in this paper.

Acknowledgements

This research was supported by Basic Science Research Program through the National Research Foundation of Korea (NRF) funded by the Ministry of Education (2022R1A6A3A03053251). This research was also partially supported by “Innovative Structural Materials Association” project through the New Energy and Industrial Technology Development Organization (NEDO) of Japan and by JST FOREST Program (Grant No. JPMJFR203W, Japan), MEXT Program Data Creation and Utilization Type Material Research and Development Project (Grant Number JPMXP1122684766), by the Ministry of Education, Culture, Sports, Science and Technology (MEXT) through a Grant- in-Aid and for Scientific Research (A) (No. 23H00229, 2023–2025, No. 20H00296, 2020–2022) and for Scientific Research (B) (No. 19H02473, 2019–2021)

Supplementary materials

Supplementary material associated with this article can be found, in the online version, at doi:10.1016/j.actamat.2024.120036.

Appendix A

The shape deformation matrix F in PTMC based on LID model is given as:

$$F = RBS_2S_1$$

where R is rigid body rotation, B is Bain deformation, S_2 is second lattice invariant shear, and S_1 is first lattice invariant shear. The values for S_2 and S_1 are adopted from the Kelly’s study [67]. The input parameters and results are summarized in Table A1. The lattice parameter at 673 K (M_s temperature) was estimated based on reported thermal expansion coefficients and empirical relations between lattice parameter and alloy elements [68-71].

Table A1
Input parameters and result data of double shear based PTMC.

Lattice parameter	$a_\gamma = 3.631$ $a_{\alpha'} = 2.888$ $c_{\alpha'} = 2.932$

(*continued on next page*)

Table A1 (*continued*)

	Lattice parameter	$a_{\gamma} = 3.631$ $a_{\alpha'} = 2.888$ $c_{\alpha'} = 2.932$
Input Parameters	S_1	(101) $[-101]_{\gamma}$ (= (112) $[-1\text{–}11]_{\alpha'}$)
	S_2	(100) $[01\text{–}1]_{\gamma}$ (= (110) $[-11\text{–}1]_{\alpha'}$)
	Magnitude of S_2	0.09122
	Bain deformation	$\begin{pmatrix} \frac{a_{\alpha'}\sqrt{2}}{a_{\gamma}} & 0 & 0 \\ 0 & \frac{a_{\alpha'}\sqrt{2}}{a_{\gamma}} & 0 \\ 0 & 0 & \frac{c_{\alpha'}}{a_{\gamma}} \end{pmatrix}$
Result	Shape strain of S_1	0.262
	Habit plane	$[0.5179, 0.7120, 0.4741]_{\gamma}$
	Shape strain direction	$[-0.2148, 0.7234, -0.6562]_{\gamma}$
	Shape strain matrix (F)	$\begin{pmatrix} 0.9743 & -0.0353 & -0.0235 \\ 0.0866 & 1.1190 & 0.0792 \\ -0.0785 & -0.1079 & 0.9281 \end{pmatrix}$
	Shape strain of F	0.231
	Orientation relationship	$(110)_{\gamma}$ - $(011)_{\alpha'}$ 0.19° deviated $[-101]_{\gamma}$ - $[-1\text{–}11]_{\alpha'}$ 3° deviated

References

[1] S. Matsuoka, H. Matsunaga, J. Yamabe, S. Hamada, T. Iijima, Various strength properties of SCM435 and SNCM439 low-alloy steels in 115 MPa hydrogen gas and proposal of design guideline, Trans. JSME 83 (854) (2017) 17–00264.

[2] L. Cho, P.E. Bradley, D.S. Lauria, M.L. Martin, M.J. Connolly, J. Benzing, E.J. Seo, K.O. Findley, J.G. Speer, A.J. Slifka, Characteristics and mechanisms of hydrogen-induced quasi-cleavage fracture of lath martensitic steel, Acta Mater. 206 (2021) 116635.

[3] L. Cho, P. Bradley, D. Lauria, M. Connolly, E. Seo, K. Findley, J. Speer, L. Golem, A. Slifka, Effects of hydrogen pressure and prior austenite grain size on the hydrogen embrittlement characteristics of a press-hardened martensitic steel, Int. J. Hydrogen Energy 46 (47) (2021) 24425–24439.

[4] Y. Momotani, A. Shibata, D. Terada, N. Tsuji, Effect of strain rate on hydrogen embrittlement in low-carbon martensitic steel, Int. J. Hydrogen Energy 42 (5) (2017) 3371–3379.

[5] K. Ogawa, Y. Matsumoto, H. Suzuki, K. Takai, Hydrogen embrittlement susceptibility evaluation of tempered martensitic steels showing different fracture surface morphologies, ISIJ Int. 59 (9) (2019) 1705–1714.

[6] T. Chen, T. Chiba, M. Koyama, A. Shibata, E. Akiyama, K. Takai, Hierarchical characteristics of hydrogen-assisted crack growth and microstructural strain evolution in tempered martensitic steels: case of quasi-cleavage fracture, Metall. Mater. Trans. A 52 (10) (2021) 4703–4713.

[7] A. Shibata, I. Gutierrez-Urrutia, A. Nakamura, K. Okada, G. Miyamoto, Y. Madi, J. Besson, T. Hara, K. Tsuzaki, Three-dimensional propagation behavior of hydrogen-related intergranular cracks in high-strength martensitic steel, Int. J. Hydrogen Energy (2023).

[8] A. Shibata, I. Gutierrez-Urrutia, A. Nakamura, G. Miyamoto, Y. Madi, J. Besson, T. Hara, K. Tsuzaki, Multi-scale three-dimensional analysis on local arrestability of intergranular crack in high-strength martensitic steel, Acta Mater. 234 (2022) 118053.

[9] K. Okada, A. Shibata, T. Sasaki, H. Matsumiya, K. Hono, N. Tsuji, Improvement of resistance against hydrogen embrittlement by controlling carbon segregation at prior austenite grain boundary in 3Mn-0.2C martensitic steels, Scr. Mater. (2022) 115043.

[10] A. Shibata, Y. Madi, K. Okada, N. Tsuji, J. Besson, Mechanical and microstructural analysis on hydrogen-related fracture in a martensitic steel, Int. J. Hydrogen Energy 44 (54) (2019) 29034–29046.

[11] A. Shibata, I. Gutierrez-Urrutia, K. Okada, G. Miyamoto, Y. Madi, J. Besson, K. Tsuzaki, Relationship between mechanical response and microscopic crack propagation behavior of hydrogen-related intergranular fracture in as-quenched martensitic steel, Mater. Sci. Eng. A 831 (2022) 142288.

[12] T. Chen, T. Chiba, M. Koyama, E. Akiyama, K. Takai, Factors distinguishing hydrogen-assisted intergranular and intergranular-like fractures in a tempered lath martensitic steel, Metall. Mater. Trans. A 53 (5) (2022) 1645–1658.

[13] A. Shibata, T. Murata, H. Takahashi, T. Matsuoka, N. Tsuji, Characterization of hydrogen-related fracture behavior in as-quenched low-carbon martensitic steel and tempered medium-carbon martensitic steel, Metall. Mater. Trans. A 46 (2015) 5685–5696.

[14] A. Nagao, C.D. Smith, M. Dadfarnia, P. Sofronis, I.M. Robertson, The role of hydrogen in hydrogen embrittlement fracture of lath martensitic steel, Acta Mater. 60 (13) (2012) 5182–5189.

[15] M. Koyama, C.C. Tasan, E. Akiyama, K. Tsuzaki, D. Raabe, Hydrogen-assisted decohesion and localized plasticity in dual-phase steel, Acta Mater. 70 (2014) 174–187.

[16] J. Han, J.-H. Nam, Y.-K. Lee, The mechanism of hydrogen embrittlement in intercritically annealed medium Mn TRIP steel, Acta Mater. 113 (2016) 1–10.

[17] H.-J. Kim, G. Shin, J. Park, M.-G. Lee, K.-J. Kim, S.-C. Yoon, Pre-strain and hydrogen charging effect on the plastic and fracture behavior of quenching and partitioning (Q&P) steel, Acta Mater. 263 (2024) 119524.

[18] H.K. Birnbaum, P. Sofronis, Hydrogen-enhanced localized plasticity—A mechanism for hydrogen-related fracture, Mater. Sci. Eng. A 176 (1) (1994) 191–202.

[19] M. Nagumo, T. Yagi, H. Saitoh, Deformation-induced defects controlling fracture toughness of steel revealed by tritium desorption behaviors, Acta Mater. 48 (4) (2000) 943–951.

[20] M. Nagumo, K. Takai, The predominant role of strain-induced vacancies in hydrogen embrittlement of steels: overview, Acta Mater. 165 (2019) 722–733.

[21] C. Liu, T. Nagoya, K. Abiko, H. Kimura, Effect of boron on the grain boundary segregation of phosphorus and intergranular fracture in high-purity Fe-0.2 Pct PB alloys, Metall. Trans. A 23 (1992) 263–269.

[22] J. Kameda, C. McMahon, The effects of Sb, Sn, and P on the strength of grain boundaries in a Ni-Cr Steel, Metall. Trans. A 12 (1981) 31–37.

[23] P. Kontis, H.M. Yusof, S. Pedrazzini, M. Danaie, K. Moore, P. Bagot, M. Moody, C. Grovenor, R. Reed, On the effect of boron on grain boundary character in a new polycrystalline superalloy, Acta Mater. 103 (2016) 688–699.

[24] S. Hwang, J. Morris, The use of a boron addition to prevent intergranular embrittlement in Fe-12Mn, Metall. Trans. A 11 (1980) 1197–1206.

[25] G.L. Krasko, G. Olson, Effect of boron, carbon, phosphorus and sulphur on intergranular cohesion in iron, Solid State Commun. 76 (3) (1990) 247–251.

[26] J. Han, A.K. da Silva, D. Ponge, D. Raabe, S.-M. Lee, Y.-K. Lee, S.-I. Lee, B. Hwang, The effects of prior austenite grain boundaries and microstructural morphology on the impact toughness of intercritically annealed medium Mn steel, Acta Mater. 122 (2017) 199–206.

[27] W. Geng, A. Freeman, G. Olson, Influence of alloying additions on grain boundary cohesion of transition metals: first-principles determination and its phenomenological extension, Phys. Rev. B 63 (16) (2001) 165415.

[28] H. Mohrbacher, T. Senuma, Alloy optimization for reducing delayed fracture sensitivity of 2000 MPa press hardening steel, Metals 10 (7) (2020) 853.

[29] C.J. McMahon, Hydrogen-induced intergranular fracture of steels, Eng. Fract. Mech. 68 (6) (2001) 773–788.

[30] K. Ito, Y. Tanaka, K. Tsutsui, T. Omura, Effect of Mo addition on hydrogen segregation at α-Fe grain boundaries: a first-principles investigation of the mechanism by which Mo addition improves hydrogen embrittlement resistance in high-strength steels, Comput. Mater. Sci. 218 (2023) 111951.

[31] W. Xing, A.R. Kalidindi, D. Amram, C.A. Schuh, Solute interaction effects on grain boundary segregation in ternary alloys, Acta Mater. 161 (2018) 285–294.

[32] M. Guttmann, Equilibrium segregation in a ternary solution: a model for temper embrittlement, Surf. Sci. 53 (1) (1975) 213–227.

[33] G. Miyamoto, A. Goto, N. Takayama, T. Furuhara, Three-dimensional atom probe analysis of boron segregation at austenite grain boundary in a low carbon steel-Effects of boundary misorientation and quenching temperature, Scr. Mater. 154 (2018) 168–171.

[34] M. Herbig, D. Raabe, Y. Li, P. Choi, S. Zaefferer, S. Goto, Atomic-scale quantification of grain boundary segregation in nanocrystalline material, Phys. Rev. Lett. 112 (12) (2014) 126103.

[35] Y. Zhang, K. Ikeda, S. Kitsuya, G. Miyamoto, T. Furuhara, Grain boundary character dependence of phosphorus segregation at ferrite grain boundaries in a high-purity iron-phosphorus binary alloy, Scr. Mater. 249 (2024) 116170.

[36] A. Jamali, A. Ma, J. Llorca, Influence of grain size and grain boundary misorientation on the fatigue crack initiation mechanisms of textured AZ31 Mg alloy, Scr. Mater. 207 (2022) 114304.

[37] F. Archie, S. Zaefferer, On variant selection at the prior austenite grain boundaries in lath martensite and relevant micro-mechanical implications, Mater. Sci. Eng. A 731 (2018) 539–550.

[38] M.H. Razmpoosh, A. Macwan, F. Goodwin, E. Biro, Y. Zhou, Crystallographic study of liquid-metal-embrittlement crack path, Mater. Lett. 267 (2020) 127511.

[39] S. Jothi, T.N. Croft, S.G.R. Brown, Influence of grain boundary misorientation on hydrogen embrittlement in bi-crystal nickel, Int. J. Hydrogen Energy 39 (35) (2014) 20671–20688.

[40] J. Yoo, M.C. Jo, M.C. Jo, S. Kim, S.-H. Kim, J. Oh, S.S. Sohn, S. Lee, Effects of solid solution and grain-boundary segregation of Mo on hydrogen embrittlement in 32MnB5 hot-stamping steels, Acta Mater. 207 (2021) 116661.

[41] T. Chen, M. Koyama, T. Chiba, E. Akiyama, K. Takai, Mesoscale quantification of grain boundary character and local plasticity in hydrogen-assisted intergranular and intergranular-like cracking paths in tempered martensitic steel, Mater. Sci. Eng. A 886 (2023) 145718.

[42] T. Furuhara, H. Kawata, S. Morito, G. Miyamoto, T. Maki, Variant selection in grain boundary nucleation of upper bainite, Metall. Mater. Trans. A 39 (5) (2008) 1003–1013.

[43] T. Kaneshita, G. Miyamoto, T. Furuhara, Variant selection in grain boundary nucleation of bainite in Fe-2Mn-C alloys, Acta Mater. 127 (2017) 368–378.

[44] S. Morito, J. Nishikawa, T. Ohba, T. Furuhara, T. Maki, The crystallography of lath martensite formed at austenite grain boundaries in Fe-Ni-Mn alloy, in: 12th International Conference on Martensitic Transformations, ICOMAT-08, 2009, pp. 649–653.

[45] Y. Shibayama, T. Hojo, E. Akiyama, An evaluation method for hydrogen embrittlement of high strength steel sheets using U-bend specimens, Isij Int. 61 (4) (2021) 1104–1111.

[46] G. Miyamoto, N. Iwata, N. Takayama, T. Furuhara, Mapping the parent austenite orientation reconstructed from the orientation of martensite by EBSD and its application to ausformed martensite, Acta Mater. 58 (19) (2010) 6393–6403.

[47] G. Miyamoto, N. Takayama, T. Furuhara, Accurate measurement of the orientation relationship of lath martensite and bainite by electron backscatter diffraction analysis, Scr. Mater. 60 (12) (2009) 1113–1116.

[48] A. Shibata, I. Gutierrez-Urrutia, A. Nakamura, T. Moronaga, K. Okada, Y. Madi, J. Besson, T. Hara, Local crack arrestability and deformation microstructure evolution of hydrogen-related fracture in martensitic steel, Corros. Sci. 233 (2024) 112092.

[49] B.W. Krakauer, D.N. Seidman, Absolute atomic-scale measurements of the Gibbsian interfacial excess of solute at internal interfaces, Phys. Rev. B 48 (9) (1993) 6724.

[50] J. Takahashi, K. Ishikawa, K. Kawakami, M. Fujioka, N. Kubota, Atomic-scale study on segregation behavior at austenite grain boundaries in boron- and molybdenum-added steels, Acta Mater. 133 (2017) 41–54.

[51] H. Aaronson, Decomposition of austenite by diffusional process, The proeutectoid ferrite and the proeutectoid cementite reaction 387 (1962).

[52] J. Ågren, Computer simulations of diffusional reactions in complex steels, ISIJ Int. 32 (3) (1992) 291–296.

[53] W. Wang, S. Zhang, X. He, Diffusion of boron in alloys, Acta Metall. et Mater. 43 (4) (1995) 1693–1699.

[54] D.H. Fors, G. Wahnström, Nature of boron solution and diffusion in α-iron, Phys. Rev. B 77 (13) (2008) 132102.

[55] H. Oikawa, Lattice diffusion in iron-a review, Tetsu-to-Hagane 68 (10) (1982) 1489–1497.

[56] M. Paju, H. Viefhaus, H.J. Grabke, Phosphorus segregation in austenite in Fe–P–C, Fe–P–B and Fe–P–C–B alloys, Steel. Res. 59 (8) (1988) 336–343.

[57] L. Karlsson, H. Norden, Overview no. 63 Non-equilibrium grain boundary segregation of boron in austenitic stainless steel—IV. Precipitation behaviour and distribution of elements at grain boundaries, Acta Metall. 36 (1) (1988) 35–48.

[58] H. Nakata, K. Fujii, K. Fukuya, R. Kasada, A. Kimura, Grain boundary phosphorus segregation in thermally aged low alloy steels, J. Nucl. Sci. Technol. 43 (7) (2006) 785–793.

[59] R. Mulford, J. McMahon, D.P. CJ, H. Feng, Temper embrittlement of Ni-Cr steels by phosphorus, Metall. Trans. A 7 (1976) 1183–1195.

[60] M. Menyhard, C.J. McMahon, On the effect of molybdenum in the embrittlement of phosphorus-doped iron, Acta Metall. 37 (8) (1989) 2287–2295.

[61] D.D. Shen, S.H. Song, Z.X. Yuan, L.Q. Weng, Effect of solute grain boundary segregation and hardness on the ductile-to-brittle transition for a Cr–Mo low-alloy steel, Mater. Sci. Eng. A 394 (1) (2005) 53–59.

[62] N. Takayama, G. Miyamoto, T. Furuhara, Effects of transformation temperature on variant pairing of bainitic ferrite in low carbon steel, Acta Mater. 60 (5) (2012) 2387–2396.

[63] S. Morito, H. Tanaka, R. Konishi, T. Furuhara, Maki, The morphology and crystallography of lath martensite in Fe-C alloys, Acta Mater. 51 (6) (2003) 1789–1799.

[64] T. Furuhara, N. Takayama, G. Miyamoto, Key factors in grain refinement of martensite and bainite, Mater. Sci. Forum Trans. Tech. Publ. (2010) 3044–3049.

[65] L. Morsdorf, C.C. Tasan, D. Ponge, D. Raabe, 3D structural and atomic-scale analysis of lath martensite: effect of the transformation sequence, Acta Mater. 95 (2015) 366–377.

[66] A.B. Greninger, The martensite thermal arrest in iron-carbon alloys and plain carbon steels, Trans. ASM 30 (1942) 1–26.

[67] P.M. Kelly, Crystallography of lath martensite in steels, Mater. Trans. 33 (3) (1992) 235–242. JIM.

[68] D. Dyson, Effect of alloying additions on the lattice parameter of austenite, J. Iron Steel Inst. 208 (1970) 469–474.

[69] L. Xiao, Z. Fan, Z. Jinxiu, Z. Mingxing, K. Mokuang, G. Zhenqi, Lattice-parameter variation with carbon content of martensite. I. X-ray-diffraction experimental study, Phys. Rev. B 52 (14) (1995) 9970.

[70] S.-J. Lee, Y.-K. Lee, Quantitative analyses of ferrite lattice parameter and solute Nb content in low carbon microalloyed steels, Scr. Mater. 52 (10) (2005) 973–976.

[71] C.G. De Andres, F.G. Caballero, C. Capdevila, H. Bhadeshia, Modelling of kinetics and dilatometric behavior of non-isothermal pearlite-to-austenite transformation in an eutectoid steel, Scr. Mater. 39 (6) (1998) 791–796.